

1 **Aerosol and Cloud Interaction Observed from High**
2 **Spectral Resolution Lidar Data**

Wenying Su,

3 Science Systems and Applications Inc., Hampton, VA, USA

Gregory L. Schuster, Norman G. Loeb,

4 NASA Langley Research Center, Hampton, VA, USA

Raymond R. Rogers,

5 Science Systems and Applications Inc., Hampton, VA, USA

Richard A. Ferrare, Chris A. Hostetler, Johnathan W. Hair

6 NASA Langley Research Center, Hampton, VA, USA

Michael D. Obland

7 Science Systems and Applications Inc., Hampton, VA, USA

W. Su, Science Systems and Applications Inc., MS420, NASA Langley Research Center, Hampton, VA 23681, USA. (Wenying.Su-1@nasa.gov)

8 **Abstract.** Recent studies utilizing satellite retrievals have shown a strong
9 correlation between aerosol optical depth (AOD) and cloud cover. However,
10 these retrievals from passive sensors are subject to many limitations, includ-
11 ing cloud adjacency (or 3D) effects, possible cloud contamination, uncertainty
12 in the AOD retrieval. Some of these limitations do not exist in High Spec-
13 tral Resolution Lidar (HSRL) observations; for instance, HSRL observations
14 are not affected by cloud adjacency effects, are less prone to cloud contam-
15 ination, and offer accurate aerosol property measurements (backscatter co-
16 efficient, extinction coefficient, lidar ratio, backscatter Angstrom exponent,
17 and aerosol optical depth) at a fine spatial resolution (< 100 m) in the vicin-
18 ity of clouds. Hence, the HSRL provides an important dataset for studying
19 aerosol and cloud interaction.

20 In this study, we statistically analyze aircraft-based HSRL profiles accord-
21 ing to their distance from the nearest cloud, assuring that all profile com-
22 parisons are subject to the same large-scale meteorological conditions. Our
23 results indicate that AODs from HSRL are about 8~17% higher in the prox-
24 imity of clouds (~ 100 m) than far away from clouds (4.5 km), which is much
25 smaller than the reported cloud 3D effect on AOD retrievals. The backscat-
26 ter and extinction coefficients also systematically increase in the vicinity of
27 clouds, which can be explained by aerosol swelling in the high relative hu-
28 midity (RH) environment and/or aerosol growth through in cloud process-
29 ing (albeit not conclusively). On the other hand, we do not observe a sys-
30 tematic trend in lidar ratio; we hypothesize that this is caused by the op-

31 positive effects of aerosol swelling and aerosol in-cloud processing on the li-
32 dar ratio. Finally, the observed backscatter Angstrom exponent (BAE) does
33 not show a consistent trend because of the complicated relationship between
34 BAE and RH. We demonstrate that BAE should not be used as a surrogate
35 for Angstrom exponent, especially at high RH.

1. Introduction

36 Several satellite studies indicate that regions with increased cloud cover are accompanied
37 by increased aerosol optical depths (AODs) in the clear areas between the clouds, and that
38 this phenomenon is occurring globally [*Sekiguchi et al.*, 2003; *Ignatov et al.*, 2005; *Loeb and*
39 *Manalo-Smith*, 2005; *Kaufman et al.*, 2005; *Matheson et al.*, 2005, 2006; *Loeb and Schuster*,
40 2008] . Possible explanations for this observed trend include cloud contamination in the
41 aerosol retrieval, aerosol swelling in the high-humidity cloudy environments [*Clarke et al.*,
42 2002], increased illumination of the cloud-free columns by the nearby clouds (i.e., the
43 cloud adjacency or 3D effect) [*Podgorny*, 2003; *Wen et al.*, 2006, 2007], increased particle
44 production in the vicinity of clouds [*Hegg et al.*, 1990; *Hoppel et al.*, 1994; *Clarke et al.*,
45 1998], and shift of aerosol size distribution to larger size because of cloud processing and
46 cloud evaporation in the vicinity of clouds [*Lelieveld and Heintzenberg*, 1992; *Alkezweeny*,
47 1995; *Hegg et al.*, 2004].

48 *Wen et al.* [2006, 2007] studied the 3D cloud radiative effects on MODIS aerosol re-
49 trievals over Brazil. Their Monte Carlo simulations indicate that ignoring the cloud ad-
50 jacency effect can cause an overestimation of 50 to 140% in AOD retrieval, with the over-
51 estimation more pronounced at shorter wavelengths. Larger increase of AOD at shorter
52 wavelengths is also shown in stochastic cloud model simulations [*Marshak et al.*, 2008].
53 They argue that the enhancement in the cloud-free column radiance comes from the en-
54 hanced Rayleigh scattering.

55 In this study, we examine the aerosol properties both in the vicinity of clouds and
56 far away from clouds using nadir-viewing aircraft-based High Spectral Resolution Lidar

57 (HSRL) profiles of aerosol backscatter and extinction coefficients. The HSRL has many
58 advantages over passive satellite instruments for observing aerosol and cloud interactions,
59 including: 1.) it provides accurate measurements of aerosol properties in the vicinity
60 of clouds as opposed to the aerosol *retrievals* provided by satellites; 2.) it is an active
61 instrument with a narrow source, so it is not affected by cloud adjacency effects; 3.) the
62 backscatter coefficient of cloud droplets is much larger than that of aerosols, so cloud
63 boundaries are readily distinguishable; and 4.) the HSRL has a spatial resolution of <
64 100 m, which makes the clear profiles less prone to cloud contamination than the much
65 larger clear pixels (≥ 500 m) associated with satellite instruments. But the disadvantage
66 of HSRL measurement is that it has limited spatial coverage and can only provide cloud
67 top height along the flight track.

2. Method

68 A standard backscatter lidar measures attenuated backscatter; retrieving extinction
69 profiles from a backscatter lidar requires the assumption of extinction-to-backscatter ratio
70 (i.e., lidar ratio). Unfortunately, the actual value of lidar ratio for tropospheric aerosols
71 can vary over a wide range (from 20 to 100 *sr*) depending on their optical properties
72 [Ansmann *et al.*, 1990; Ackermann, 1998; Anderson *et al.*, 2000; Ferrare *et al.*, 2001;
73 Cattrall *et al.*, 2005], which leads to large uncertainty in the retrieved aerosol extinction.
74 Unlike a standard backscatter lidar, the HSRL provides measurements of both aerosol
75 extinction and backscatter, which enables the robust computation of the lidar ratio.

76 In this section, first we describe the NASA Langley Research Center (LaRC) airborne
77 HSRL, then we describe our statistical analysis of HSRL data. We compare each HSRL
78 clear profile to a clear profile next to clouds (i.e., reference profile); this analysis method

79 ensures that both the clear profile and the reference profile are subject to the same large-
80 scale meteorological conditions. For a given flight, aerosol properties of all clear profiles
81 and differences between clear profiles and reference profiles are binned by clear profiles'
82 distances to the nearest clouds. For each bin, average differences are presented and possible
83 causes for the differences are analyzed.

2.1. Description of LaRC HSRL

84 The LaRC HSRL instrument and its measurement technique is described in *Hair et al.*
85 [2006], which we briefly review here. The basic concept of HSRL measurements is to
86 obtain the lidar return signal with high spectral resolution (< 75 MHz laser bandwidth),
87 which enables the separation of aerosol and cloud returns from molecular returns. This
88 separation is possible because the spectrum of the molecular backscatter is Doppler broad-
89 ened by the thermal motion of the molecules, whereas Doppler broadening of the aerosol
90 and cloud backscatter is negligible because of the much slower thermal velocities of the
91 aerosol/cloud particles. The separation of molecular from aerosol/cloud backscatter en-
92 ables the independent retrieval of aerosol/cloud backscatter and extinction profiles. An-
93 other key feature of the LaRC HSRL is the ability to calibrate the instrument internally,
94 thereby eliminating systematic errors associated with vicarious calibration in regions that
95 are assumed to have negligible aerosol loading.

96 The LaRC HSRL includes three measurement channels at the 532 nm wavelength and
97 two measurement channels at the 1064 nm wavelength; parallel and perpendicular scat-
98 tering channels are included at both wavelengths, and an additional channel for molecular
99 scattering is included at the 532 nm wavelength. The molecular channel makes it possible
100 to derive reliable aerosol backscatter (β) and extinction (σ) profiles at 532 nm, and hence

101 the aerosol lidar ratio: $S_a = \sigma/\beta$. A lidar ratio is assumed to derive extinction profiles
 102 for the 1064 nm wavelength (although a more sophisticated algorithm incorporating the
 103 532 nm lidar ratio could be implemented in the future).

Two additional parameters can be derived from the HSRL measurements. The aerosol depolarization ratio can be calculated from the perpendicular and parallel backscatter at both wavelengths: $\delta = \beta^\perp/\beta^\parallel$. We also define the backscatter Angstrom exponent (BAE, analogous to the Angstrom exponent):

$$BAE = \frac{-\ln(\beta_{1064}/\beta_{532})}{\ln(2)}, \quad (1)$$

104 where the denominator represents the logarithm of the wavelength ratio. The absolute
 105 uncertainties of these HSRL observed variables used in this study are listed in Table 1.

2.2. Statistical Analysis Method

106 The LaRC HSRL was deployed on the LaRC's King Air B-200 aircraft during the
 107 CATZ ¹ campaign over the Eastern United States (June 26 to August 29, 2007). One of
 108 the objectives of this campaign was to investigate the nature of particles in the 'twilight
 109 zone' between clouds and aerosols [*Koren et al.*, 2007]. The aircraft flew at an altitude
 110 of 9 km, and measurements were averaged over 100 shots (0.5 sec) in the lidar electronics
 111 before being transferred to a laptop computer. Within 0.5 sec, HSRL usually covers a
 112 spatial resolution of 50–75 m, depending upon the flight speed of the aircraft (which varies
 113 somewhat during each flight). The vertical resolution of backscatter and extinction are
 114 30 m and 300 m, respectively.

CALIPSO (Cloud-Aerosol Lidar and Infrared Pathfinder Satellite Observation) AERONET (Aerosol Robotic Network) Twilight Zone

115 As our objective is to understand changes in aerosol optical properties in the vicinity
116 of boundary layer clouds, we must first determine the proximity of the lidar beam to
117 a cloud boundary. We identify cloud top altitudes for clouds located at or near the
118 top of the planetary boundary layer using background subtracted, range-square-corrected
119 profiles from the HSRL. A three point Haar wavelet covariance transform [*Gamage and*
120 *Hagelberg, 1993*] is used to detect the sharp gradients in these HSRL profiles associated
121 with cloud boundaries.

122 Thus, the location of clouds along the flight track can be easily determined using HSRL
123 data, but the HSRL cannot provide information about clouds that are not directly under-
124 neath the aircraft. The ideal flight tracks for our aerosol and cloud interaction study are
125 those that have almost no clouds on either side of the clear portions on the tracks. We
126 visually inspected Geostationary Operational Environmental Satellites (GOES) images
127 obtained during the CATZ campaign to identify those ideal cases, and chose segments
128 of flights on August 4th, 7th, and 9th for our study. Note the spatial resolution of GOES
129 visible images is 1 km; therefore subpixel clouds may still be nearby. Backscatter profiles
130 of the time periods used in this analysis for the three days are shown in Fig. 1. The
131 August 4th flight segment covers a distance of about 250 km from Maryland to Virginia
132 with AOD around 0.4, the August 7th flight segment covers a distance of about 560 km
133 off the coast of North Carolina with AOD around 0.7, and the August 9th flight segment
134 covers a distance of about 200 km off the coast of South Carolina with AOD around 0.9.

135 Next, we choose a reference altitude of the low clouds (H_c) for each flight segment
136 ($H_c = 2000$ m, 500 m, and 500 m for August 4th, 7th, and 9th, respectively), and analyze
137 all of the clear HSRL profiles at this altitude. We define a profile as being ‘clear’ if it does

138 not have a valid cloud top height but has valid backscatter and extinction measurements
139 over the entire altitude range. We define a profile as being ‘cloudy’ if it has a valid cloud
140 top height between H_c and $H_c + 200$ m, assuming that the geometrical thickness of the
141 boundary layer clouds is about 200 m [Bennartz, 2007]. However, we also tested cloud
142 geometrical thickness of 500 m and 1000 m, which did not change the general trends of
143 our results.

144 Then we save the aerosol optical properties (β, σ, S_a, BAE) in each clear profile (x_i),
145 and search the temporal record to identify the closest cloudy profile (x_j) that occurs
146 before or after x_i . Since x_j is the nearest cloudy profile, any profile (such as x_{j+1} and
147 x_{j+2}) between it and x_i is clear. We are interested in how aerosol properties in the near-
148 cloud environment differ from the aerosol properties in the far-cloud environment, so we
149 also note the aerosol optical properties in a clear profile x_{j+2} , which is ~ 100 m from
150 x_j . Hereafter, x_{j+2} is referred to as reference profile. We choose x_{j+2} instead of x_{j+1}
151 to reduce the possibility of cloud contamination that could occur in profiles that are too
152 close to clouds (x_{j+1} is about ~ 50 m away from x_j). Nonetheless, our analysis produces
153 statistically equivalent results when using x_{j+1} or x_{j+2} for the near-cloud reference profile,
154 which is a testament to the robustness of the cloud screening technique used for the HSRL
155 data.

156 We calculate the difference in aerosol optical properties between profile x_i and reference
157 profile x_{j+2} (for example, $\delta\beta = \beta_i - \beta_{j+2}$, where β_{j+2} is the near-cloud reference value) and
158 the difference is binned according to the distance between x_i and x_j . Here we consider
159 seven bins, which are listed in Table 2, along with the total number of samples in each

bin for the three days analyzed in this study. For each bin, the averaged difference
 ($\overline{\delta\beta}, \overline{\delta\sigma}, \overline{\delta S_a}, \overline{\delta BAE}$) and the standard error for each aerosol property are calculated.

3. Results

Figure 2 shows the averaged differences for 532 nm backscatter coefficient ($\overline{\delta\beta}$, in unit
 $Mm^{-1}sr^{-1}$) for the three days. The averaged near-cloud reference backscatter coefficients
 ($\overline{\beta_{j+2}}$) are also included. The error bars for each bin in Figure 2 are given by the standard
 error of that bin, calculated as the standard deviation of the differences divided by the
 square root of the number of samples of that bin. Figure 2 indicates systematic increases
 in β as clear profiles get closer to clouds. For example, on August 4th, $\overline{\beta_{j+2}}$ is about 1.2
 $Mm^{-1}sr^{-1}$ (23%) higher than the averaged backscatter coefficient in the second distance
 bin (501–1000 m away from nearest clouds); and $\overline{\beta_{j+2}}$ is about 1.4 $Mm^{-1}sr^{-1}$ (27%)
 higher than the averaged backscatter coefficient in the seventh distance bin (4001–5000 m
 away from nearest clouds). The other two days show similar increasing trends of β as the
 clear profiles get closer to clouds. $\overline{\beta_{j+2}}$ is about 30% and 26% higher than the averaged
 backscatter coefficient in the seventh bin for August 7th and 9th.

The uncertainty of the averaged difference in each bin associated with the instrumental
 error can be calculated by dividing the instantaneous uncertainty, listed in Table 1, by
 the square root of the total number of samples of that bin. For example, the instrumental
 error in $\overline{\delta\beta}$ is about 0.06 $Mm^{-1}sr^{-1}$ for the first bin on August 4th. The $\overline{\delta\beta}$ shown in
 Figure 2 is much larger than the instrumental error for all the bins on the three days,
 which indicates that the systematic trend is not affected by random instrumental error.

180 Depolarization ratios at 532 nm during these three days are less than 0.02 and exhibit
181 nearly no changes in the vicinity of clouds, indicating that there are very few non-spherical
182 dust particles.

183 The extinction coefficients at 532 nm for the three days are qualitatively similar to
184 backscatter coefficients (figure not shown). For clear profiles in the second bin, the av-
185 eraged extinction coefficients are about 0.10, 0.06, and 0.10 km^{-1} lower than those near-
186 cloud reference values and correspond to 24%, 10%, and 13% decreases. The differences
187 are 0.17, 0.10, and 0.17 km^{-1} for clear profiles in the seventh bin and correspond to 42%,
188 17%, and 23% decreases. Again, the averaged extinction differences in all bins for the
189 three days are much larger than the instrumental errors.

190 Aerosol optical depth (AOD) can be computed by integrating the HSRL measured
191 extinction profiles between the surface and the flight altitude of 6.5 km. Differences
192 between AODs that are near and far from clouds are analyzed using the same method.
193 Figure 3 shows the averaged differences for AOD at 532 nm ($\overline{\delta AOD}$). Averaged near-
194 cloud reference AODs are also listed. AODs from profiles in the second distance bin are
195 0.03, 0.02 and 0.07 lower than those near-cloud reference values, on August 4th, 7th, and
196 9th, respectively. These correspond to 6%, 3%, and 8% decreases relative to the reference
197 AODs. AODs from profiles in the seventh distance bin are 0.04, 0.06, and 0.16 (9%, 8%,
198 and 17%) lower than the near-cloud reference AODs. The averaged AOD differences in
199 all bins for the three days are much larger than the instrumental errors.

200 Figure 4 shows the averaged differences for the 532 nm lidar ratio ($\overline{\delta S_a}$) for the three
201 days. Unlike the systematic decreases seen in β , σ , and AOD as clear profiles get farther
202 away from clouds, we do not see any consistent changes in $\overline{\delta S_a}$ (except for those between

203 2000 and 5000 m away from the nearest clouds on August 4th). Note the instrumental
204 error in $\overline{\delta S_a}$ for some bins with small number of samples can be up to 3 *sr*, which could be
205 responsible for some of the variability seen in Figure 4. We also notice that the averaged
206 near-cloud reference lidar ratios are ~ 80 *sr* for the three days that we investigated.
207 Since the lidar ratio for water clouds is significantly lower (~ 18 *sr*) [*Pinnick et al.*,
208 1983; *O'Connor et al.*, 2004], this once again shows that our results are not affected by
209 significant cloud contamination.

210 Figure 5 shows the averaged differences for the BAE, and the averaged near-cloud
211 reference BAEs. The trends of BAE are mixed. On August 4th, no systematic changes of
212 BAEs are observed within 1500 m of clouds. Thereafter the BAEs decrease by about 0.05
213 to 0.14 (5% to 13% relative to the near-cloud value) as the clear profiles get farther away
214 from the nearest clouds. On August 7th, BAEs exhibit systematic increases as the clear
215 profiles move farther away from clouds. BAEs increase by about 0.15 to 0.09 (12% to 8
216 %) for clear profiles that are between 2000 and 5000 m away from the nearest clouds. On
217 August 9th, there is no systematic changes in BAEs.

4. Discussion

218 The increased backscatter and extinction coefficients observed with the HSRL in the
219 vicinity of clouds are not caused by cloud adjacency effects or cloud contamination; we
220 know this because of the advantages of HSRL measurements outlined in Section 1 (i.e.,
221 narrow field of view and high sensitivity to differences in scattering caused by aerosols and
222 cloud drops). Other possible causes include: 1.) new particle production in the vicinity
223 of clouds; 2.) aerosol growth through in-cloud aqueous oxidation of SO₂ to sulfate and

224 collision/coalescence; and 3.) aerosol swelling as relative humidity (RH) increases near
225 clouds.

226 New particle production in the vicinity of clouds alters the aerosol size distribution.
227 *Hegg et al.* [1990] noted that aerosol number size distribution in the vicinity of clouds
228 consists of more smaller particles ($r < 0.05\mu m$) than the nearby clear air aerosol size
229 distribution, and suggested that this is due to homogeneous heteromolecular nucleation.
230 *Hoppel et al.* [1994] observed a large number of small particles ($r < 0.01\mu m$) above the
231 cloud top and interpreted this as an evidence of new particle formation. *Clarke et al.*
232 [1998] also observed significant increase of ultra fine particles ($0.002 < r < 0.005\mu m$) at
233 the edges of clouds. However, given the very small size of these particles, they are unlikely
234 to affect the measured extinction and backscatter coefficients [*Schuster et al.*, 2006].

235 Aerosol growth near clouds has been observed in both *in situ* measurements and model
236 simulations. *Alkezweeny* [1995] measured a decreased aerosol number concentration for
237 optically active aerosols with radii below $0.2\mu m$, and an increased aerosol number concen-
238 tration for aerosol radii between 0.2 and $1.5\mu m$ in the processed clear air. He argued that
239 the in-cloud chemical conversion of SO_2 to sulfate adds new material to droplet. Since
240 every droplet generates only one aerosol particle upon evaporation [*Mitra et al.*, 1992], the
241 new size is therefore larger. Although *Alkezweeny* [1995] did not measure particle sizes
242 greater than $1.5\mu m$, we note that the increase in particle number concentrations altered
243 the particle size distribution of the coarse mode ($r \gtrsim 0.5\mu m$) as well as the accumulation
244 mode.

245 *Hegg et al.* [2004] observed enhanced light-scattering efficiency in the vicinity of clouds,
246 and attributed the enhancement to a shift in the aerosol size distribution toward a more

247 effective scattering size range. *Feingold and Kreidenweis* [2002] used a large eddy simula-
248 tion to demonstrate that aqueous chemistry increased the aerosol number concentration
249 for radii between 0.1 and 1.5 μm (no data were shown beyond 1.5 μm). *Kerkweg et al.*
250 [2003] used an air-parcel model to demonstrate that aqueous chemistry and coalescence of
251 cloud droplets enhanced the number of larger aerosol particles ($r > 2 \mu m$) in the processed
252 aerosol size distribution.

253 Swelling of aerosols in the high RH environment can alter their optical properties and
254 possibly their size distribution depending on their composition. We investigate the ob-
255 served near- and far-cloud differences in aerosol optical properties by simulating aerosol
256 hygroscopic growth, following the method outlined in *Loeb and Schuster* [2008]. That
257 is, we assume that the aerosols in our study are an equilibrium mixture [*Tang, 1996*] of
258 ammonium sulfate and water in the fine mode and sea salt (or dust) in the coarse mode,
259 and that the size distribution is represented by the GSFC climatology of *Dubovik et al.*
260 [2002]. Then we use Mie theory [*Wiscombe, 1980*] to compute the backscatter, extinction,
261 lidar ratio, and backscatter Angstrom exponent.

262 The backscatter coefficient (β) and lidar ratio (S_a) are plotted in Figures 6 and 7 at
263 four dry fine volume fractions, assuming sea salt occupies the coarse mode. The results
264 for dust in the coarse mode are qualitatively similar, except that the sensitivity of the
265 lidar ratio to dry fine volume fraction is smaller at high RH. Since the hygroscopic growth
266 factor is different for the fine and coarse modes in our simulations (owing to the different
267 composition of the two modes), the *wet* fine volume fraction changes along the curves in
268 Figures 6 and 7, even though the *dry* fine volume fraction remains the same. Hereafter,
269 all fine volume fractions in our discussion refer to dry fine volume fractions. If aerosol

270 swelling in the vicinity of clouds is the only mechanism altering the β and S_a , the aerosol
271 properties are expected to follow a single curve. However, if aerosol growth through in-
272 cloud processing alters the relative distribution of the fine and coarse modes, then β and
273 S_a will move from one curve to another in Figures 6 and 7.

274 Figure 6 shows the simulated backscatter coefficient (β) as a function of RH for four
275 dry fine volume fractions; β increases by a factor of two as RH increases from 55% to
276 90%, and thereafter it increases sharply. In fact, β at 99% RH is more than an order
277 of magnitude larger than at 55% RH. Also note that β is not sensitive to fine volume
278 fraction for RH less than 97%, especially for aerosols dominated by the fine mode (like
279 pollution). The relationship between extinction coefficient and RH is qualitatively similar
280 to our backscatter coefficient simulation (figure not shown); the extinction coefficient is
281 also not sensitive to the fine volume fraction when RH is less than 97%.

282 Figure 6 clearly indicates that aerosol swelling is consistent with the unambiguous in-
283 crease of backscatter and extinction coefficients observed in the vicinity of clouds (Figure
284 2). In addition, aerosol growth through in-cloud processing (which enhances the aerosol
285 light-scattering efficiency), can also increase backscatter and extinction in the vicinity of
286 clouds.

287 The unambiguous increase of extinction coefficients also translates to the increase of
288 column aerosol optical depths at 532 nm in the vicinity of clouds. AODs increase by about
289 8% to 17% in the vicinity of clouds than far away from clouds (4.5 km). *Koren et al.*
290 [2007] found that AOD at 440 nm decreased by about $13\% \pm 2\%$ on average from the first
291 sample measured near a cloud to the second sample (less than 15 minutes later). In their
292 study, multiple years of data from 15 AERONET stations were used, and the boundary

293 layer wind speed data were not always available at these stations to translate the time
294 interval between these two samples to geometrical distance. However, if we assume a
295 boundary layer wind speed of 4.96 m s^{-1} [the globally averaged daytime 80-m wind speed
296 from *Archer and Jacobson, 2005*], we can approximate the distance between these two
297 samples to be $\sim 4.5 \text{ km}$. Although the wind speed we use here is a crude approximation,
298 it nonetheless shows that AOD increases in the vicinity of clouds at nearly the same
299 magnitude for both the *Koren et al. [2007]* study and our study. The AOD increase in
300 the vicinity of clouds from these two studies (which are not affected by cloud adjacency
301 effects) is much smaller than the cloud adjacency effects on AOD retrieval (50 to 140%
302 overestimation) [*Wen et al., 2006, 2007*].

303 The simulated lidar ratio (S_a) also increases as dry fine volume fraction and RH increase,
304 as shown in Figure 7. If aerosol swelling is the only mechanism affecting our HSRL
305 measurements in the vicinity of clouds, then S_a should increase near clouds, which is
306 not consistent with our observations; two out of three days shown in Figure 4 do not
307 exhibit any systematic trend in S_a . One possible explanation is aerosol growth caused by
308 oxidation of SO_2 and collision/coalescence increases the relative fraction of coarse mode
309 aerosols in the vicinity of clouds. Since S_a is smaller for coarse mode aerosols than for
310 fine mode aerosols, this counteracts the enhancement in S_a caused by aerosol swelling;
311 hence, the non-systematic trend in Figure 4. Unfortunately, we do not have simultaneous
312 aerosol size and RH measurements to verify this hypothesis.

313 The simulated BAE increases as fine volume fraction at a given RH (as expected), but
314 the relationship between RH and BAE is not monotonic (figure not shown). BAE first
315 decreases as RH increases, until a certain RH (96% and 90%, respectively, for fine volume

316 fraction of 0.3 and 1), then BAE increases. Therefore, depending on the RH values next
317 to clouds and away from clouds, and the aerosol properties along the flight tracks, the
318 BAE differences shown in Figure 5 can be explained by aerosol swelling and growth. This
319 once again stresses the importance of concurrent RH and aerosol property measurements.

320 To investigate if BAE could be used as a surrogate for Angstrom exponent (AE), we
321 present BAE as a function of AE for four dry fine volume fractions as RH increases
322 from 55% to 99% in Figure 8, using sea salt for the coarse mode. The AE is defined for
323 wavelengths 553 and 855 nm, which are the same wavelengths used for one of the MODIS'
324 AEs over the ocean [Remer *et al.*, 2005]. For RH less than $\sim 85\%$, BAE and AE are linearly
325 correlated for aerosol size distributions dominated by the fine mode (BAE decreases as
326 AE decreases). As aerosols continue to swell, however, the BAE increases while the AE
327 decreases. Also, the BAE and AE are anti-correlated for coarse mode dominated aerosols
328 over the RH range considered here. Therefore, the humidification trends of BAE and AE
329 are not similar, and BAE should not be used as a surrogate for Angstrom exponent. Also,
330 the information content about the aerosol size distribution in the BAE is very limited, as
331 also shown by Feingold and Grund [1994].

5. Summary

332 We used aircraft HSRL measurements to study aerosol and cloud interaction during the
333 CATZ campaign. Unlike satellite retrievals, HSRL observations are not affected by cloud
334 adjacency effects, and offer accurate measurements of aerosol properties in the vicinity of
335 clouds. (The aerosol properties investigated in this study include aerosol backscatter and
336 extinction coefficients, lidar ratios, backscatter Angstrom exponents, and column aerosol
337 optical depths.) The HSRL also provides robust cloud screening, and we used GOES

338 images to select observational periods with very few low clouds on both sides of the flight
339 tracks, thereby minimizing the effects of clouds that do not appear in the lidar beam.

340 We examined the aerosol properties of HSRL profiles in the vicinity of clouds according
341 to the distance from the nearest clouds, observing differences between clear profiles that
342 are adjacent to clouds (~ 100 m from clouds) and clear profiles that are up to 5000 m away
343 from clouds. The short distance between these profiles (< 5000 m) assures the same large-
344 scale meteorological condition for both profiles, which is important for studying aerosol
345 and cloud interactions [Loeb and Manalo-Smith, 2005; Mauger and Norris, 2007; Loeb and
346 Schuster, 2008].

347 Results from three observations in August 2007 reveal unambiguous increases of
348 backscatter coefficients, extinction coefficients, and aerosol optical depths in the vicin-
349 ity of clouds. These increases are possibly caused by aerosol swelling and aerosol growth
350 in the vicinity of clouds. However, we do not observe any systematic lidar ratio changes in
351 the vicinity of clouds. We hypothesize that changes in S_a are neutralized by the opposite
352 effects of aerosol swelling associated with a high relative humidity environment (which
353 increases S_a), and aerosol growth associated with cloud processing (which decreases S_a
354 if the aerosol size distribution shifts to the coarse mode). We do not observe systematic
355 changes of BAE in the vicinity of clouds, either. Theoretical simulations reveal that the
356 relationship between BAE and RH is rather complicated, and that it would be rather diffi-
357 cult to infer changes in the aerosol size distribution from BAE. Furthermore, BAE should
358 not be used as a surrogate for Angstrom exponent, especially at high relative humidity.

359 **Acknowledgments.** The authors thank the support from NASA CALIPSO program
360 and NASA Interdisciplinary Research in Earth Science under the direction of Dr. Hal

361 Maring. The authors are grateful to Bill Smith Jr. for discussions on GOES image. At
362 the time this research was performed, Michael Obland was a NASA postdoctoral fellow
363 at NASA Langley Research Center, administered by Oak Ridge Associated Universities
364 through a contract with NASA.

References

- 365 Ackermann, J. (1998), The extinction-to-backscatter ratio of tropospheric aerosol: a num-
366 berical study, *J. Atmos. Oceanic Technol.*, *15*, 1043–1050.
- 367 Alkezweeny, A. J. (1995), Field observations of in-cloud nucleation and the modification
368 of atmospheric aerosol size distribution after cloud evaporation, *J. Appl. Meteor.*, *34*,
369 2649–2654.
- 370 Anderson, T. L., S. J. Masonis, D. S. Covert, R. J. Charlson, and M. J. Rood (2000), In
371 situ measurement of the aerosol extinction-to-backscatter ratio at a polluted continental
372 site, *J. Geophys. Res.*, *105*(D22), 26,907–26,915.
- 373 Ansmann, A., M. Riebesell, and C. Weitkamp (1990), Measurement of atmospheric aerosol
374 extinction profiles with a raman lidar, *Opt. Lett.*, *15*, 746–748.
- 375 Archer, C. L., and M. Z. Jacobson (2005), Evaluation of global wind power, *J. Geophys.*
376 *Res.*, *110*(D12110), doi:10.1029/2004JD005462.
- 377 Bennartz, R. (2007), Global assessment of marine boundary layer cloud droplet number
378 concentration from satellite, *J. Geophys. Res.*, *112*(D02201), doi:10.1029/2006JD007547.
- 379 Cattrall, C., J. Reagan, K. Thome, and O. Dubovik (2005), Variability of aerosol
380 and spectral lidar and backscatter and extinction ratios of key aerosol types derived
381 from selected aerosol robotic network locations, *J. Geophys. Res.*, *110*(D10S11), doi:
382 10.1029/2004JD005124.
- 383 Clarke, A. D., J. L. Varner, F. Eisele, R. L. Mauldin, and D. Tanner (1998), Particle
384 production in the remote marine atmosphere: Cloud outflow and subsidence during ace
385 1, *J. Geophys. Res.*, *103*(D13), 16,397–16,409.

- 386 Clarke, A. D., S. Howell, P. K. Quinn, T. S. Bates, J. A. Ogren, and coauthors (2002),
387 INDOEX aerosol: A comparison and summary of chemical, microphysical, and optical
388 properties observed from land, ship, and aircraft, *J. Geophys. Res.*, *107*(8033), doi:
389 10.1029/2001JD000572.
- 390 Dubovik, O., B. Holben, T. Eck, A. Smirnov, Y. Kaufman, M. King, D. Tanre, and
391 I. Slutsker (2002), Variability of absorption and optical properties of key aerosol types
392 observed in worldwide locations, *J. Atmos. Sci.*, *59*, 590–608.
- 393 Feingold, G., and C. J. Grund (1994), Feasibility of using multiwavelength lidar measure-
394 ments to measure cloud condensation nuclei, *J. Atmos. Oceanic Technol.*, *11*, 1543–1558.
- 395 Feingold, G., and S. M. Kreidenweis (2002), Cloud processing of aerosol as modeled by
396 a large eddy simulation with coupled microphysics and aqueous chemistry, *J. Geophys.*
397 *Res.*, *107*(D23, 4687), doi:10.1029/2002JD002054.
- 398 Ferrare, R. A., D. D. Turner, L. H. Brasseur, W. F. Feltz, O. Dubovik, and T. P.
399 Tooman (2001), Raman lidar measurements of the aerosol extinction-to-backscatter
400 ratio over the southern great plains, *J. Geophys. Res.*, *106*, 20,333–20,348, doi:
401 10.1029/2000JD000144.
- 402 Gamage, N., and C. Hagelberg (1993), Detection and analysis of microfronts and associ-
403 ated coherent events using localized transforms, *J. Atmos. Sci.*, *50*(5), 750–756.
- 404 Hair, J. W., C. A. Hostetler, R. A. Ferrare, A. L. Cook, and D. B. Harper (2006), The
405 nasa langley airborne high spectral resolution lidar for measurements of aerosols and
406 clouds, in *Proceedings of 23rd International Laser Radar Conference (ILRC)*, edited by
407 C. Nagasawa and N. Sugimoto, pp. 411–414.

- 408 Hegg, D. A., L. F. Radke, and P. V. Hobbs (1990), Particle production associated with
409 marine clouds, *J. Geophys. Res.*, *95*(D9), 13,917–13,926.
- 410 Hegg, D. A., D. S. Covert, H. Jonsson, D. Khelif, and C. A. Friehe (2004), Observations
411 of the impact of cloud processing on aerosol light-scattering efficiency, *Tellus*, *56B*,
412 285–293.
- 413 Hoppel, W. A., G. M. Frick, J. W. Fitzgerald, and R. E. Larson (1994), Marine boundary
414 layer measurements of new particle formation and the effects nonprecipitating clouds
415 have on aerosol size distribution, *J. Geophys. Res.*, *99*(D7), 14,443–14,459.
- 416 Ignatov, A., P. Minnis, N. Loeb, B. Wielicki, W. Miller, S. Sun-Mack, D. Tanre, L. Remer,
417 I. Laszlo, and E. Geier (2005), Two MODIS aerosol products over ocean on the terra
418 and aqua CERES SSF datasets, *J. Atmos. Sci.*, *62*, 1008–1031.
- 419 Kaufman, J. Y., I. Koren, L. A. Remer, D. Rosenfeld, and Y. Rudich (2005), The effect
420 of smoke, dust, and pollution aerosol on shallow cloud development over the atlantic
421 ocean, *Proc. Natl. Acad. Sci.*, *102*(32), 11,207–11,212.
- 422 Kerkweg, A., S. Wurzler, T. Reisin, and A. Bott (2003), On the cloud processing of
423 aerosol particles: an entraining air-parcle model with two-dimensional spectral cloud
424 microphysics and a new formulation of the collection kernel, *Quart. J. Roy. Meteorol.*
425 *Soc.*, *129*(587), 1–18.
- 426 Koren, I., L. A. Remer, Y. J. Kaufman, Y. Rudich, and J. V. Martins (2007), On
427 the twilight zone between clouds and aerosols, *Geophys. Res. Lett.*, *34*(L08805), doi:
428 10.1029/2007GL029253.
- 429 Lelieveld, J., and J. Heintzenberg (1992), Sulfate cooling effect on climate through in-cloud
430 oxidation of anthropogenic SO₂, *Science*, *258*, 117–120.

- 431 Loeb, N. G., and N. Manalo-Smith (2005), Top-of-atmosphere direct radiative effect of
432 aerosols over global oceans from merged CERES and MODIS observations, *J. Climate*,
433 *18*, 3506–3526.
- 434 Loeb, N. G., and G. L. Schuster (2008), An observational study of the relationship between
435 cloud, aerosol and meteorology in broken low-level cloud conditions, *J. Geophys. Res*,
436 *113*(accepted).
- 437 Marshak, A., G. Wen, J. A. C. Jr., L. A. Remer, N. G. Loeb, and R. F. Cahalan (2008),
438 A simple model for the cloud adjacency effect and the apparent bluing of aerosols near
439 clouds, *J. Geophys. Res*, *submitted*.
- 440 Matheson, M. A., J. A. C. Jr., and W. R. Tahnk (2005), Aerosol and cloud prop-
441 erty relationships for summertime stratiform clouds in the northeastern atlantic from
442 advanced very high resolution radiometer observations, *J. Geophys. Res*, *110*, doi:
443 10.1029/2005JD006165.
- 444 Matheson, M. A., J. A. C. Jr., and W. R. Tahnk (2006), Multiyear advance very high reso-
445 lution radiometer observations of summertime stratocumulus collocated with aerosols in
446 the northeastern atlantic, *J. Geophys. Res*, *111*(D15206), doi:10.1029/2005JD006890.
- 447 Mauger, G. S., and J. R. Norris (2007), Meteorological bias in satellite estimates of aerosol-
448 cloud relationships, *Geophys. Res. Lett.*, *34*(L16824), doi:10.1029/2007GL029952.
- 449 Mitra, S. K., J. Brinkmann, and H. R. Juppacher (1992), A wind tunnel study on the
450 drop-to-particle conversion, *J. Aerosol Sci.*, *23*, 245–256.
- 451 O’Connor, E. J., A. J. Illingworth, and R. J. Hogan (2004), A technique for autocalibration
452 of cloud lidar, *J. Atmos. Oceanic Technol.*, *21*, 777–786.

- 453 Pinnick, R. G., S. G. Jennings, P. Chylek, C. Ham, and W. T. G. Jr (1983), Backscatter
454 and extinction in water clouds, *J. Geophys. Res.*, *88*, 6787–6796.
- 455 Podgorny, I. A. (2003), Three-dimensional radiative interactions in a polluted broken
456 cloud system, *Geophys. Res. Lett.*, *30*(14), 1771–1774, doi:10.1029/2003GL017287.
- 457 Remer, L. A., Y. Kaufman, D. Tanre, S. Mattoo, D. A. Chu, J. V. Martins, and coauthors
458 (2005), The MODIS aerosol algorithm, products, and validation, *J. Atmos. Sci.*, *62*,
459 947–973.
- 460 Schuster, G. L., O. Dubovik, and B. N. Holben (2006), Angstrom exponent and bimodal
461 aerosol size distributions, *J. Geophys. Res.*, *111*(D07207), doi:10.1029/2005JD006328.
- 462 Sekiguchi, M., T. Nakajima, K. Suzuki, K. Kawamoto, A. Higurashi, D. Rosenfeld, I. Sano,
463 and S. Mukai (2003), A study of the direct and indirect effects of aerosols using global
464 satellite data sets of aerosol and cloud parameters, *J. Geophys. Res.*, *108*(D22, 4699),
465 doi:10.1029/2002JD003359.
- 466 Tang, I. (1996), Chemical and size effects of hygroscopic aerosols on light scattering coef-
467 ficients, *J. Geophys. Res.*, *101*(D14), 19,245–19,250.
- 468 Wen, G., A. Marshak, and R. F. Cahalan (2006), Impact of 3d clouds on clear sky re-
469 flectance and aerosol retrievals in biomass burning region of brazil, *Geosci. Remote*
470 *Sens. Lett.*, *3*, 169–172.
- 471 Wen, G., A. Marshak, R. F. Cahalan, L. A. Remer, and R. G. Kleidman (2007), 3-d
472 aerosol-cloud radiative interaction observed in collocated MODIS and ASTER images
473 of cumulus cloud fields, *J. Geophys. Res.*, *112*(D13204), doi:10.1029/2006JD008267.
- 474 Wiscombe, W. (1980), Improved mie scattering algorithms, *Appl. Opt.*, *19*(9), 1505–1509.

Table 1. Estimated instantaneous uncertainties for HSRL observed variables at 532 nm: backscatter (β), extinction (σ), lidar ratio (S_a), depolarization (δ), backscatter Angstrom Exponent (BAE), and aerosol optical depth (AOD).

Variable	Uncertainty
$\beta(Mm^{-1}sr^{-1})$	0.36
$\sigma(km^{-1})$	0.055
$S_a(sr^{-1})$	14
δ	0.009
BAE	0.007
AOD	0.05

Table 2. Distances of the seven bins from the nearest clouds, and total number of samples of each bin for the three days.

Bin number	1	2	3	4	5	6	7
Distance (m)	1–500	501–1000	1001–1500	1501–2000	2001–3000	3001–4000	4001–5000
N (08/04)	37	29	24	20	26	27	25
N (08/07)	362	200	108	60	90	70	62
N (08/09)	246	120	75	52	55	25	24

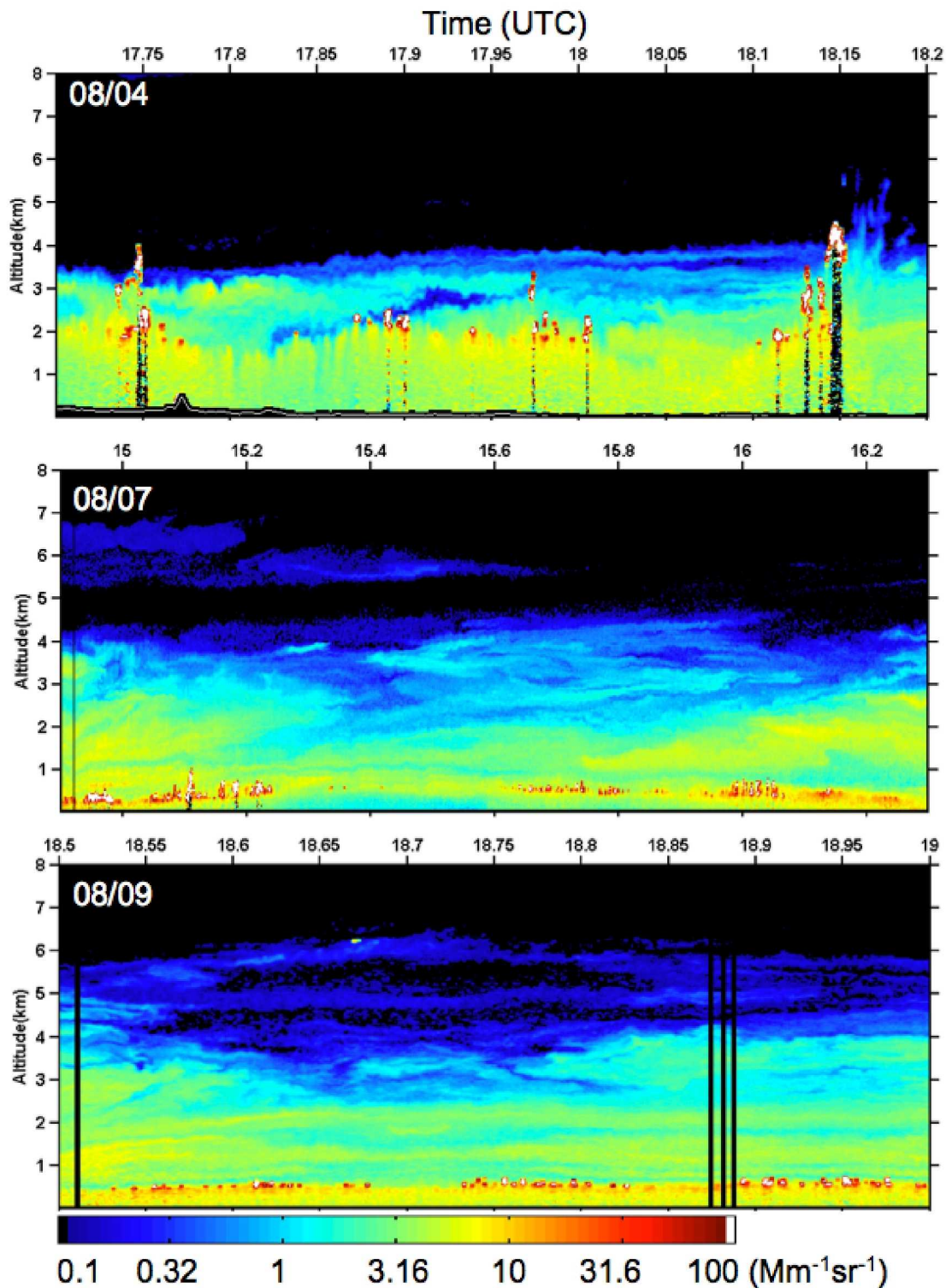


Figure 1. Backscatter coefficient profiles at 532 nm for the periods used in this analysis on August 4th, 7th, and 9th, 2007.

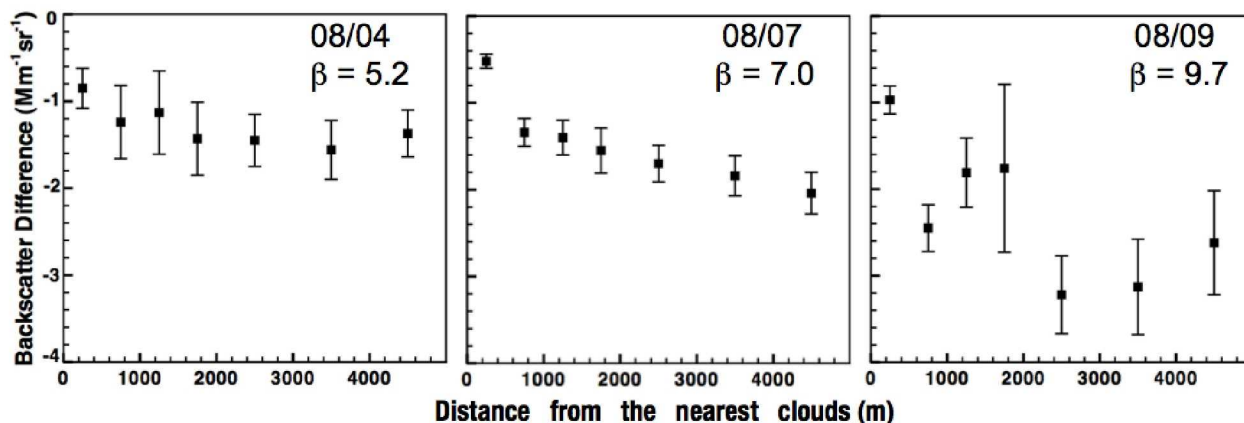


Figure 2. Average 532 nm backscatter differences ($\overline{\delta\beta}$) as a function of distance to nearest clouds on Aug. 4th, 7th, and 9th, 2007. Error bar for each bin is the standard error of that bin, calculated as the standard deviation of the difference divided by the square root of the number of samples of that bin. Averaged near-cloud reference backscatter coefficients are also included in the figure. Negative differences indicate that far-cloud values are less than near-cloud values.

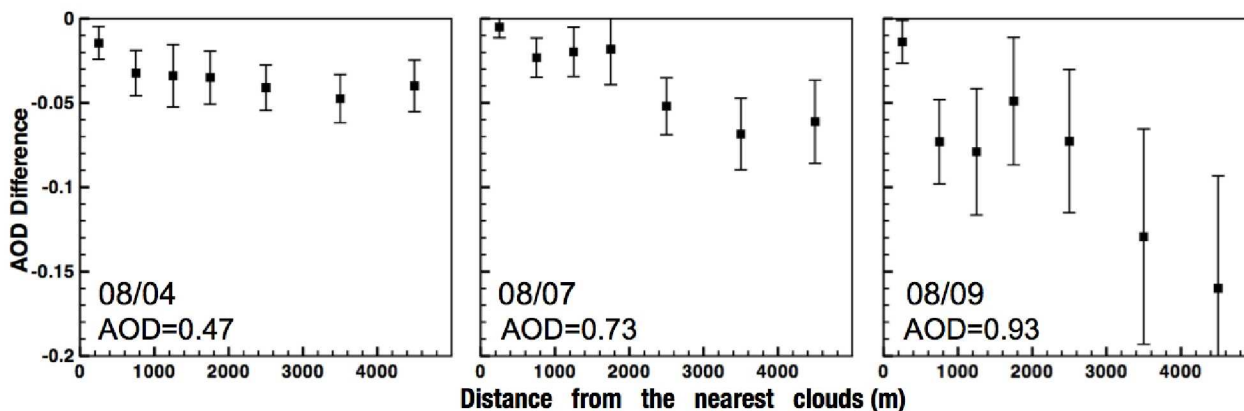


Figure 3. Average aerosol optical depth differences ($\overline{\delta AOD}$) as a function of distance to nearest cloud on Aug. 4th, 7th, and 9th, 2007. Error bar stands for the standard error. Average near-cloud reference AODs are also included in the figure. Negative differences indicate that far-cloud values are less than near-cloud values.

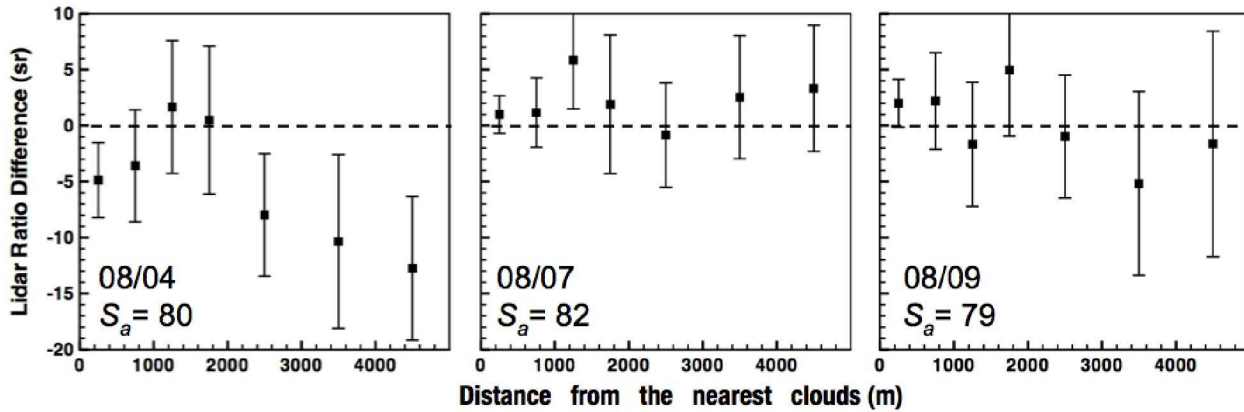


Figure 4. Average 532 nm lidar ratio differences ($\overline{\delta S_a}$) as a function of distance to nearest cloud on Aug. 4th, 7th, and 9th, 2007. Error bar stands for the standard error. Average near-cloud reference lidar ratios are also included in the figure. Negative differences indicate that far-cloud values are less than near-cloud values.

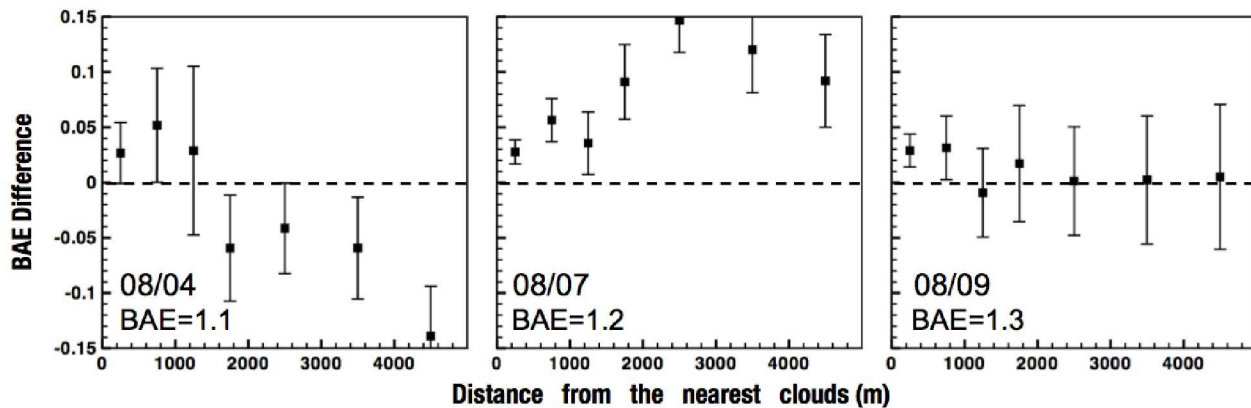


Figure 5. Average backscatter Angstrom exponent differences ($\overline{\delta BAE}$) as a function of distance to nearest cloud on Aug. 4th, 7th, and 9th, 2007. Error bar stands for the standard error. Average near-cloud reference BAEs are also included in the figure. Negative differences indicate that far-cloud values are less than near-cloud values.

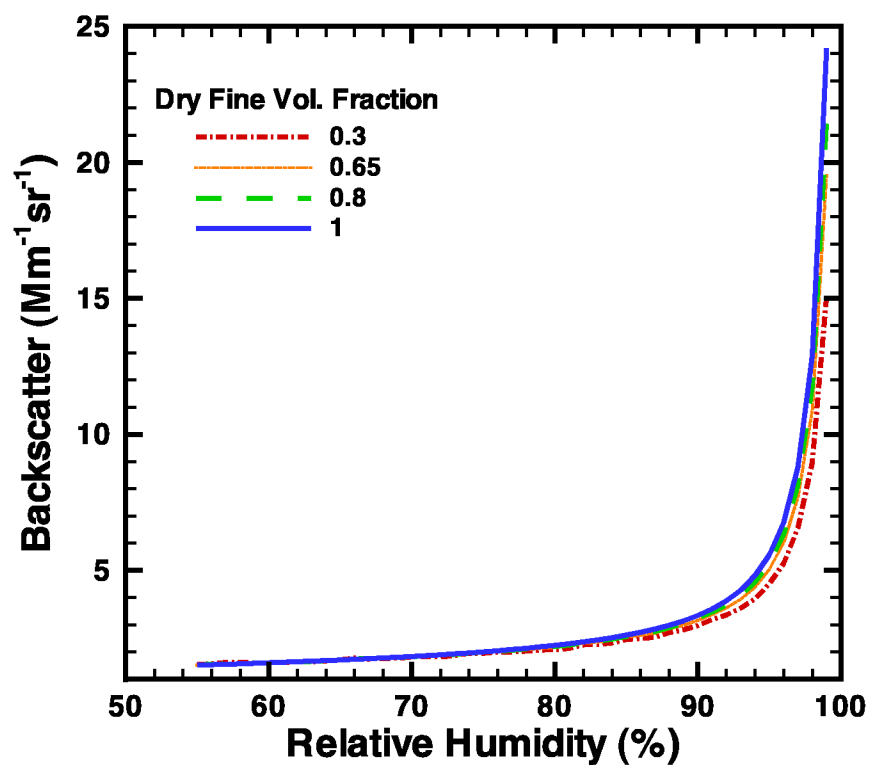


Figure 6. Backscatter coefficient as a function of relative humidity calculated using Mie theory based on GSFC climatology for four dry fine mode volume fractions. (Note that the wet fine volume fractions change along these curves.)

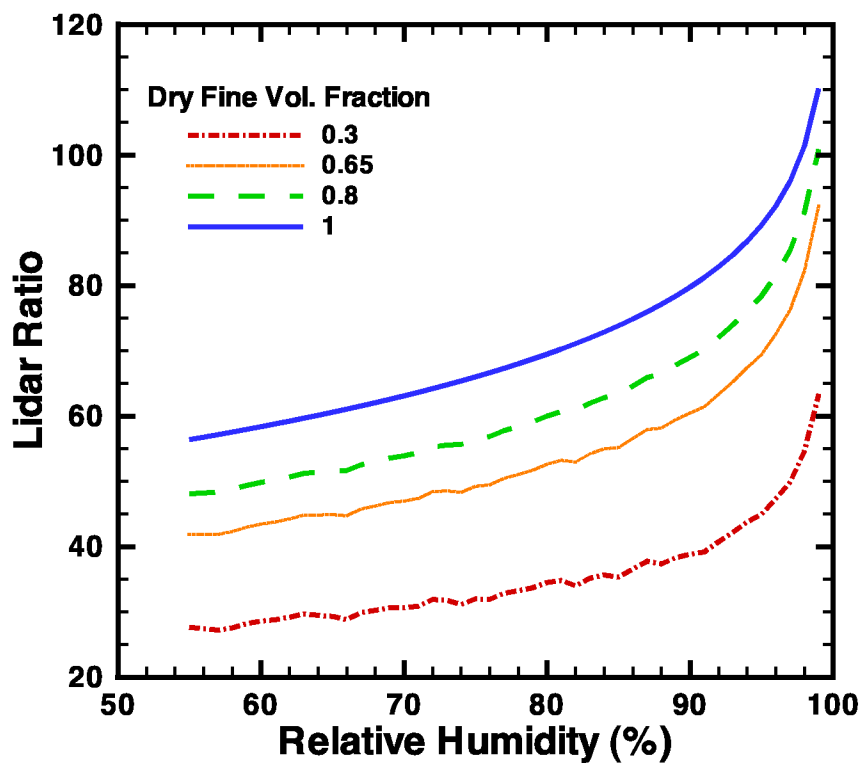


Figure 7. Lidar ratio as a function of relative humidity calculated using Mie theory based on GSFC climatology for four dry fine mode volume fractions.

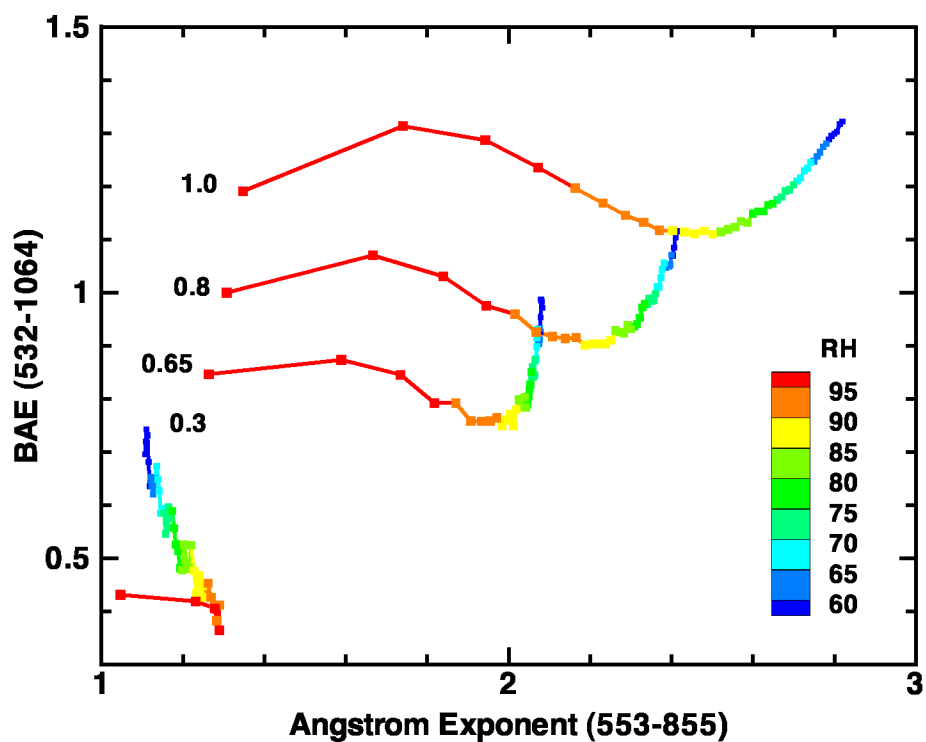


Figure 8. Relationship between backscatter Angstrom exponent for wavelength 532 nm and 1064 nm and Angstrom exponent for 553nm and 855 nm for four dry fine volume fractions as RH increases from 55% to 99%.